

## Research

# Low mutual coupling miniaturized dual-band quad-port MIMO antenna array using decoupling structure for 5G smartphones

Rania Hamdy Elabd<sup>1</sup> · Ahmed Jamal Abdullah Al-Gburi<sup>2</sup>

Received: 20 October 2023 / Accepted: 28 February 2024

Published online: 04 April 2024

© The Author(s) 2024 [OPEN](#)

## Abstract

Maintaining the compactness of 5G smartphones while accommodating millimeter-wave (mm-wave) bands presents a significant challenge due to the substantial difference in frequency. To tackle this issue, we introduce a miniaturized quad-port dual-band multiple-input, multiple-output (MIMO) antenna with low mutual coupling (MC) and a considerable frequency difference. This quad-port MIMO antenna, built on a Rogers TMM4 substrate, measures  $17.76 \times 17.76 \text{ mm}^2$  and boasts a dielectric constant of 4.5. It incorporates four planar patch antennas, positioned at the corners in perpendicular orientations. For dual-band operation at 28/38 GHz, each antenna element features a rectangular patch with four rectangular slots, complemented by a full ground plane. The spacing between these elements is  $0.5 \lambda_0$ , and we've included a decoupling structure (DS) to minimize mutual coupling (MC) among the MIMO antenna elements with minimal complexity and cost. Simulation and measurement results reveal a significant reduction in mutual coupling between the array elements, ranging from  $-25$  to  $-60$  dB. As a result, we've developed the envelope correlation coefficient (ECC) and made advancements in the total active reflection coefficient (TARC), mean effective gain (MEG), and diversity gain (DG). The measured gains for this design are approximately 8.9 dBi at both 28 GHz and 38 GHz, with a radiation efficiency of nearly 93%. Furthermore, specific absorption rate (SAR) analysis confirms the MIMO antenna's suitability for smartphone handsets operating within the target frequency band.

**Keywords** 5G smartphone · MIMO antenna · Decoupling structure (DS) · Mutual coupling (MC) · Millimeter-wave (mm-wave) · Specific absorption rate (SAR) · Equivalent circuit model

## 1 Introduction

The rapid evolution of fifth-generation (5G) technology has brought about substantial enhancements in wireless communication networks. These improvements encompass reduced latency, increased data throughput, enhanced connectivity, and better spectral efficiency [1–3]. Among the pivotal elements in 5G wireless devices, MIMO antenna technology plays a crucial role, widely adopted in numerous systems to meaningfully boost channel capacity [4, 5].

Millimeter-wave (mm-Wave) communication presents numerous benefits over current wireless technologies, such as significantly wider bandwidths, greater spectrum availability, and reduced component sizes [6, 7]. The Federal

---

✉ Ahmed Jamal Abdullah Al-Gburi, ahmedjamal@utem.edu.my; ahmedjamal@ieee.org | <sup>1</sup>Electronic and Communication Department, Higher Institute of Engineering and Technology in New Damietta, Damietta 34517, Egypt. <sup>2</sup>Center for Telecommunication Research & Innovation (CeTRI), Fakulti Teknologi dan Kejuruteraan Elektronik dan Komputer (FTKEK), Universiti Teknikal Malaysia Melaka (UTeM), Jalan Hang Tuah Jaya, Durian Tunggal, 76100 Melaka, Malaysia.



Communications Commission (FCC) has allocated frequencies at 28 GHz, 37 GHz, 39 GHz, and 64–71 GHz for fifth-generation (5G) applications [8].

Antenna scientists have been driven to design antennas with elevated gain and wideband characteristics to combat the effects of route loss and atmospheric absorption, which result in signal attenuation within these frequency ranges [9–13]. Additionally, incorporating a greater number of antenna elements offers advantages such as increased system capacity, improved signal transmission quality, and a reduction in multipath issues [14–16]. However, achieving effective MC between these elements poses a challenge for MIMO antenna designers, as heightened MC within the wanted frequency range can lead to a decrease in antenna performance [17, 18]. Consequently, embracing a MIMO configuration with robust isolation among antenna elements can enhance the overall system's performance. This improvement encompasses the ability to attain high data rates, expand capacity, mitigate multipath interference, and enhance system reliability [19–21].

Recently, researchers have developed multiple MIMO antennas that operate at dual bands of 28/38 GHz. In [10], the authors describe a dual-band 27/39 GHz MIMO antenna consisting of two elements, achieving isolation levels exceeding 25 dB and a peak gain of approximately 5 dBi. Meanwhile, in [15], they discuss a dual-band circularly polarized quad-port antenna that operates at 28/38 GHz, providing about 36 dB of isolation and a peak gain exceeding 7 dBi. In [22], a two-element MIMO antenna working at 28/38 GHz is presented with 30 dB of isolation and a simulated peak gain of 7 dBi. Furthermore, [23] suggests a circularly polarized two-port MIMO antenna based on an artificial neural network (ANN) for the dual bands of 28/38 GHz. In [24], the authors introduce a two-port MIMO antenna for the same bands, achieving isolation greater than 25 dB and a peak gain of around 1.7 dBi. Further, [25] studies a quad-port MIMO antenna operating at 28/37 GHz. [26] presents a two fold-element MIMO antenna working at 28/38 GHz with MC exceeding 20 dB. In [27], a quad-port dual-band 28/38 GHz antenna is achieved with a peak gain of more than 7 dBi and isolation of over 20 dB. In [28], the authors illustrate a quad-port antenna operating at 28/38 GHz with around 25 dB of isolation and a peak gain exceeding 5 dBi. Moreover, in [29], a quad-element MIMO antenna for the dual bands of 28/38 GHz is realized with 30 dB of MC and a simulated peak gain of 9 dBi. Finally, in [30], a two-port MIMO SIW antenna for the dual bands of 28/38 GHz is proposed, featuring a peak gain greater than 5 dBi. In [31], the researchers explore a four-element MIMO/array antenna designed for dual-band operation at 28/38 GHz, and their simulations indicate a peak gain of 9 dBi. Meanwhile, in [32], the authors detail the development of a six-port loop antenna working at the dual bands of 28/38 GHz, demonstrating more than 25 dB of isolation and a simulated peak gain surpassing 4.5 dBi.

The primary obstacle when creating a MIMO array is managing MC, which can impact the array's radiation pattern. In an array, the level of MC is inversely linked to the spacing among the individual antenna elements. Consequently, numerous investigations have delved into a variety of strategies to tackle this challenge [34–54]. For instance, researchers in [34, 35] employed the EBG approach to enhance isolation, while [36–38] utilized the DGS approach to address this issue. Furthermore, several studies [39, 40] applied the NL technique to confront this problem, and [41] utilized the parasitic element approach. Some authors [42] also implemented the decoupling method when analyzing these structures.

In order to improve its performance and attain the targeted dual-band operation at 28/38 GHz, we have incorporated a single-element design based on [33] for our investigation. We have made essential alterations to the dimensions and customized the shape accordingly. Subsequently, we have developed a four-port orthogonal MIMO antenna arrangement, utilizing a dielectric substrate (DS) technique to minimize mutual coupling. This antenna configuration is capable of accommodating 5G millimeter-wave frequencies at 28/38 GHz and provides four dual-band channels.

To maintain affordability and simplicity in the antenna's construction, we have utilized a Rogers TMM4 substrate with a dielectric constant of 4.5 and a thickness of 1.52 mm. The overall size of the MIMO antenna is  $17.76 \times 17.76 \text{ mm}^2$ , with a peak gain of 8.9 dBi and an efficiency of approximately 93%. Notably, increasing the number of elements by a factor of two continues to effectively reduce mutual coupling.

In brief, this paper's main contributions can be outlined as follows:

- The suggested quad-port MIMO antenna designed for dual-band operation spans across two frequency ranges: from 27.66 GHz to 28.378 GHz for the first band and from 37.7 GHz to 38.26 GHz for the second band. This compact antenna has a total dimension of  $17.76 \times 17.76 \text{ mm}^2$ .
- Mutual coupling (MC) is enhanced by introducing orthogonal shapes combined with four strandlines and integrating them with four single antenna elements. This configuration provides high isolation, especially at 28 GHz, reaching – 60 dB due to a decoupling structure (DS) technique placed between antenna elements.
- A comprehensive equivalent circuit model is introduced to validate the design process for both the single and four-port MIMO antennas.

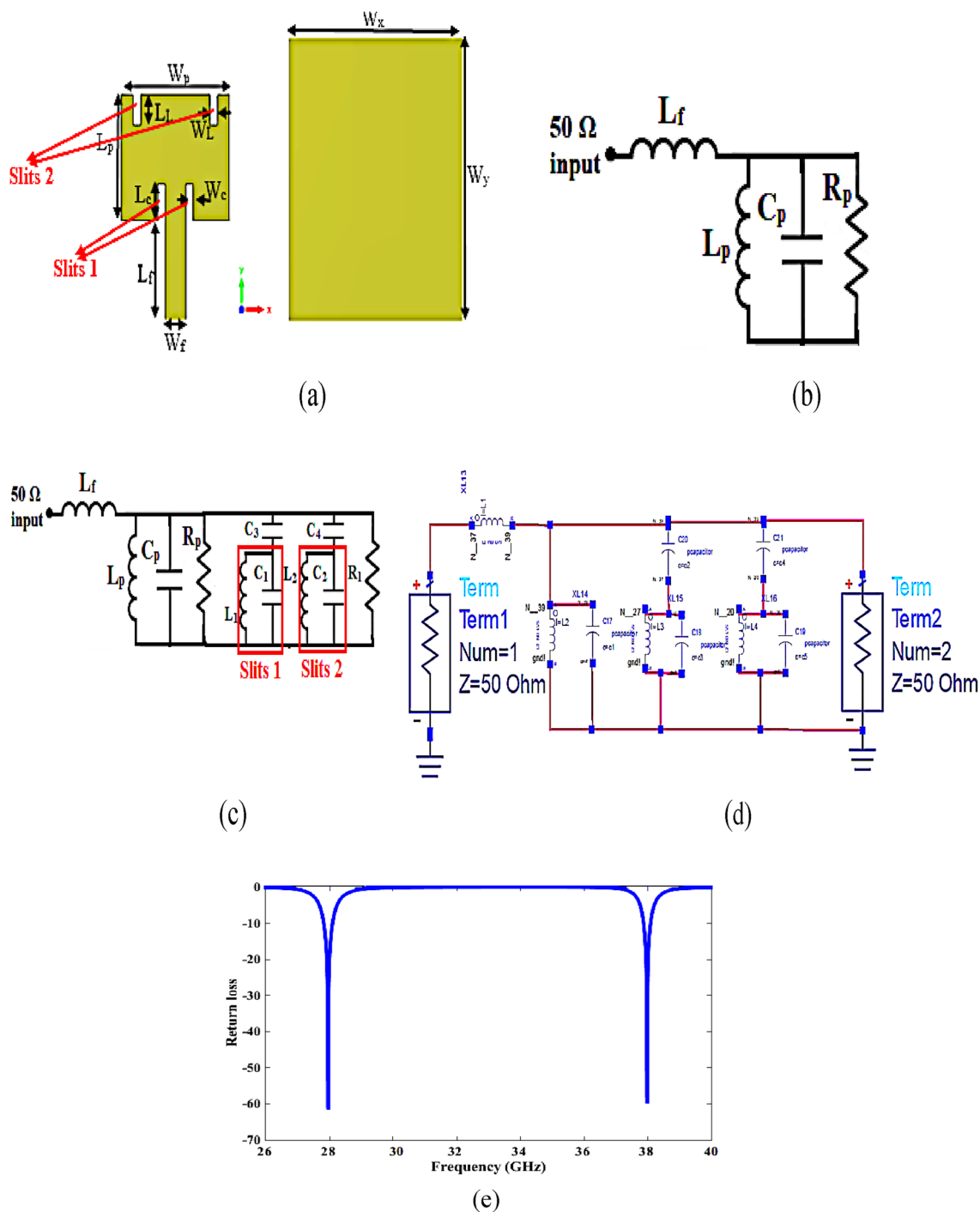


**Fig. 1** An individual patch antenna’s geometry. **a** Top view, **b** bottom view, **c** equivalent circuit of conventional antenna, **d** equivalent circuit of proposed antenna, **e** schematic diagram on ADS program, and **e** Return loss of the antenna derived from the equivalent circuit

- An elaborate time-domain analysis is also conducted to validate the radiation efficiency of the proposed antenna design for 5G millimeter-wave signal propagation, which achieved 93%.
- Specific absorption rate (SAR) analysis is conducted to verify the performance of the MIMO antenna for smartphone handsets.

## 2 Antenna setup and design

As illustrated in Fig. 1 (a), the idea behind the suggested antenna is to use a quadrilateral patch antenna with four rectangular holes etched from the radiating element and a full ground plane to accomplish the necessary twofold band 28/38 GHz. The dimension of the prototype antenna is  $W_x \times W_y = 8.88 \times 8.88 \text{ mm}^2$ . On a Rogers TMM4 substrate with a 4.5 dielectric constant, the antenna is printed. The width of the patch controls the antenna's bandwidth. The patch antenna's length  $L_p$  and width  $W_p$  are computed using the equations listed below [33]:

$$W_p = \frac{C}{4f_o \sqrt{\frac{\epsilon_r + 1}{2}}} \quad (1)$$

$$L_p = \frac{C}{4f_o \sqrt{\epsilon_{eff}}} \quad (2)$$

$$\epsilon_{eff} = \frac{\epsilon_r + 1}{2} + \frac{\epsilon_r - 1}{2} \frac{1}{\sqrt{1 + 12 \frac{h}{W_p}}} \quad (3)$$

Here,  $h$  denotes the substrate's height on the Rogers TMM4. The terms  $\epsilon_{eff}$ ,  $C$ , and  $f_o$  stand for effective permittivity, ( $3 \times 10^8$  m/s) light speed, and center frequency, respectively.

The electrical model serves as a valuable tool for comprehending how the antenna functions, presenting its operation through equivalent lump elements for clearer visualization. A resonator can be represented as a parallel RLC circuit, as indicated in reference [54]. Following a similar approach, we've created a simplified equivalent circuit model for a traditional single element, as depicted in Fig. 1(b). In this model, the patch antenna is approximated using an RLC circuit, where 'R' corresponds to the radiation resistance of the antenna's radiating mode, and 'L' and 'C' characterize the resonant circuit responsible for achieving the desired resonant frequency. The lower and upper two rectangular slits represents LC circuit ( $L_1$  and  $C_1$ ) for lower and ( $L_2$  and  $C_2$ ) for upper, connected with antenna through capacitor  $C_3$  and  $C_4$ , respectively as shown in Fig. 1(c). the antenna element is excited by a separate  $50 \Omega$  terminal.

The equivalent circuit model was optimized in Key sight Advance Design System (ADS) as shown in Fig. 1(d). The component values in the circuit model are illustrated as follows:  $L_f = 9.4 \text{ pH}$ ,  $L_p = 10.6 \text{ pH}$ ,  $C_p = 3.85 \text{ pF}$ ,  $R_p = 50 \Omega$ ,  $C_1 = 0.2 \text{ pF}$ ,  $L_1 = 9.4 \text{ pH}$ ,  $C_2 = 8.4 \text{ pF}$ ,  $L_2 = 10.4 \text{ pH}$ ,  $C_3 = 2 \text{ pF}$ ,  $C_4 = 0.6 \text{ pF}$ , and  $R_1 = 50 \Omega$ .

The return loss derived from the circuit model are corroborated through comprehensive full-wave simulation analysis, as depicted in Fig. 1(e).

Equation (4) provides the equivalent admittance of the parallel resonance:

$$Y = \frac{1}{R_p} + j2\pi \left( C_p f - \frac{1}{4\pi^2 L_p f} \right) \quad (4)$$

Since  $Z = 1/Y$ , subsequently, the equivalent impedance is expressed as follows:

$$Z = \frac{1}{\frac{1}{R_p} + j2\pi \left( C_p f - \frac{1}{4\pi^2 L_p f} \right)} \quad (5)$$

To determine the equivalent circuit parameters ( $R_p$ ,  $L_p$ , and  $C_p$ ), we apply the following formulas:

$$S21 = \frac{1}{1 + \frac{1}{2} Z Z_0^{-1}} \quad (6)$$

$$S21 = \frac{2Z_0}{2Z_0 + \left[ \frac{1}{R_p} + j2\pi \left( C_p f - \frac{1}{4\pi^2 L_p f} \right) \right]^{-1}} \quad (7)$$

Fig. 2 Design phases of the dual-band antenna. a Ant 1, b Ant 2, and c Ant 3

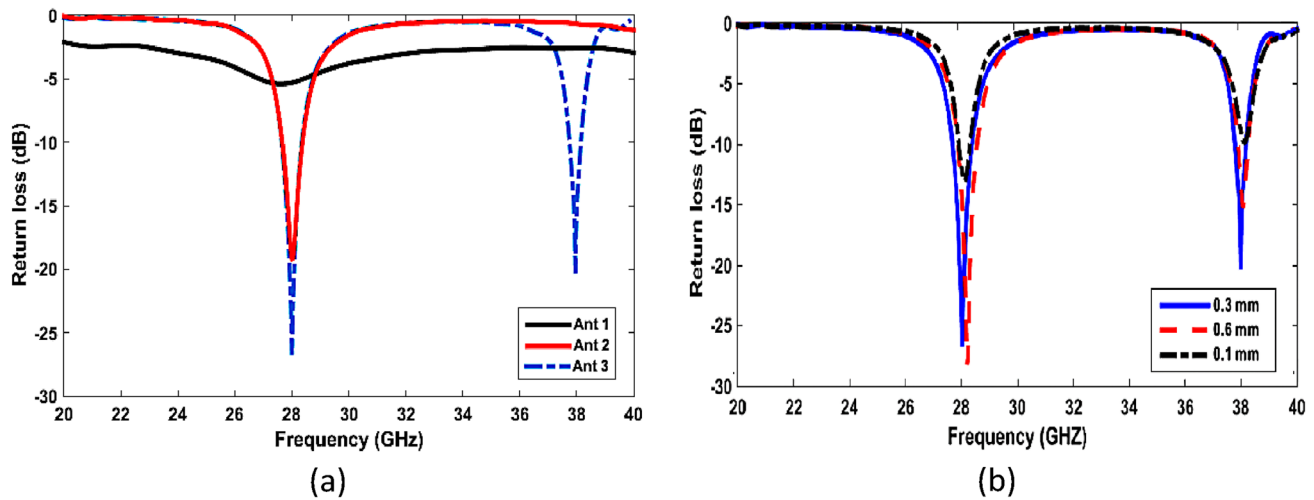
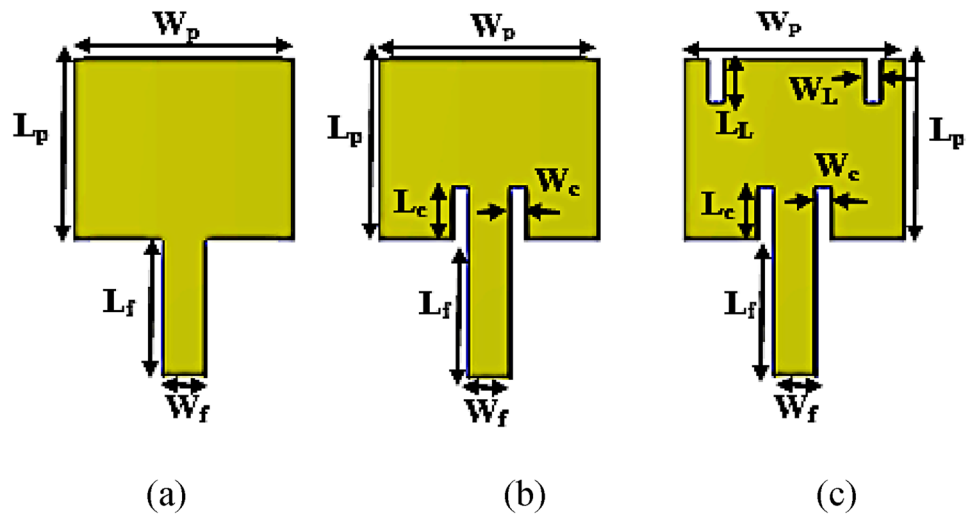


Fig. 3 Simulated return loss a for three design phases of a single element, and b for different values of  $W_c$

Table 1 Antenna specifications, with all measurements provided in millimeters (mm)

Variable	Value (mm)	Variable	Value (mm)	Variable	Value (mm)	Variable	Value (mm)
$W_y$	8.88	$W_p$	4.24	$W_L$	0.3	$W_c$	0.3
$W_x$	8.88	$L_p$	3.47	$L_L$	0.83	$L_c$	1

Supposing that  $\gg Z_0$ , we obtain:

$$S_{21} = \frac{2Z_0}{2Z_0 + \left[ j2\pi(C_p f - \frac{1}{4\pi^2 L_p f}) \right]^{-1}} \tag{8}$$

At a -3 dB point, which corresponds to the cutoff frequency  $f_c$ , we observe the following:

$$|S_{21}| = \frac{2Z_0}{\sqrt{4Z_0^2 + \left( \frac{\omega_c}{C_p(\omega_0^2 - \omega^2)} \right)^2}} = \frac{1}{\sqrt{2}} \tag{9}$$

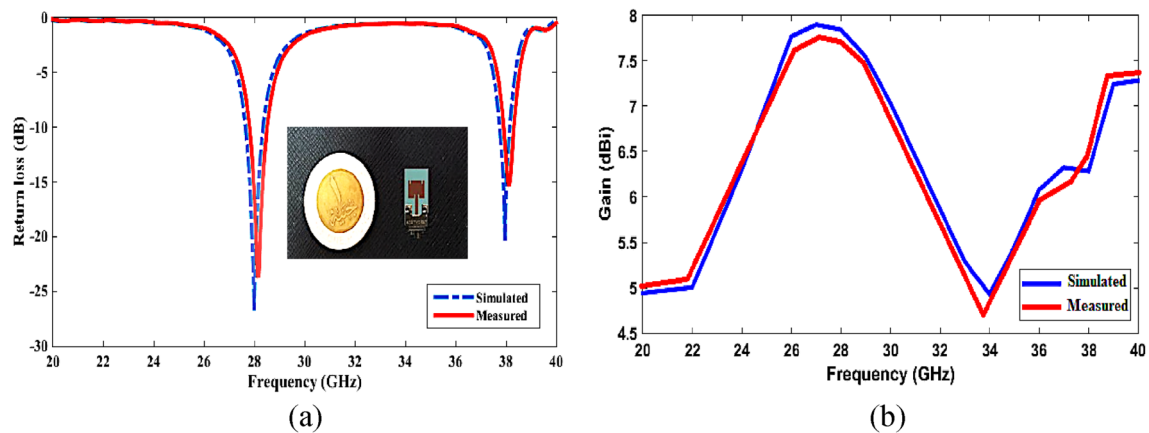


Fig. 4 Predicated and measured outcomes of a single antenna element **a** Return loss, and **b** gain

Here,  $\omega_c$  represents the angular frequency at cutoff, and  $\omega_0$  signifies the angular frequency at resonance. By employing Eqs. (8) and (9), we can derive the values for the capacitance and inductance of the equivalent circuit:

$$C_p = \frac{\omega_c}{2Z_0(\omega_0^2 - \omega_c^2)} \tag{10}$$

$$L_p = \frac{2Z_0(\omega_0^2 - \omega_c^2)}{\omega_c\omega_0^2} \tag{11}$$

The resistance 'R' in the equivalent circuit is most appropriately adjusted in the vicinity of the resonance frequency. Under these conditions, the equivalent impedance ' $Z_e$ ' is equal to 'R', and the relationship is expressed as follows:

$$S_{21}|_{\omega=\omega_0} = \left| \frac{2Z_0}{2Z_0 + Z_e} \right| = \frac{2Z_0}{2Z_0 + R_p} \tag{12}$$

Then,

$$R_p = \frac{2Z_0(1 - S_{21}|_{\omega=\omega_0})}{S_{21}|_{\omega=\omega_0}} \tag{13}$$

Figure 2 depicts the single element antenna's three primary design phases. The initial design for the first stage (Ant1) is a rectangular radiating patch with dimensions of  $W_p \times L_p = 4.24 \times 3.47 \text{ mm}^2$ . The patch is fed using a 50 microstrip line with the dimensions  $W_f$  and length  $L_f$ .

By etching two rectangular slots of the same length on the radiating element on either side of the feed line, the second stage (Ant 2) achieves the first resonance mode 28 GHz. The final stage (Ant. 3), which will produce the second resonance mode at 38 GHz, is etching two rectangular slots of the same length at the top of the radiating element at equal distances from the sides. Figure 3 displays the outcomes of the three design steps using CST Microwave Studio 2019. We have four rectangular slots for obtaining a 28/38 GHz twofold-band antenna, as was previously stated in Ant 3. Figure 3(a) showed the three antennas' reflection coefficients as a function of frequency. The  $S_{11}$  simulation output for ant 1 (black color) is greater than  $-10$  dB. The initial resonance at 28 GHz can be found by switching to ant 2 (red color), and its  $S_{11}$  is  $-20$  dB. For ant 3 (blue color), the dual band is seen at 28/38 GHz, and its  $S_{11}$  for these frequencies is, respectively,  $-27.1$  dB and  $-23.8$  dB. Table 1 provides the optimal antenna dimensions.

As shown in Fig. 2(c), the addition of the slits enhances the frequency band that covers the two resonance frequency. It is observed that the  $S_{11}$  values are less than  $-10$  dB at 28/38GHz. We observed a close match between the equivalent circuit and proposed single element.

Extensive parametric investigations into the width of the slits have been conducted for the designed antenna, and these studies have revealed a significant impact of the width ( $W_c$ ) on the antenna's directivity. The return loss has been

**Fig. 5** The geometry of a MIMO antenna array, shown in **a** from the top view, **b** from the bottom view, and **c** represented as its equivalent circuit

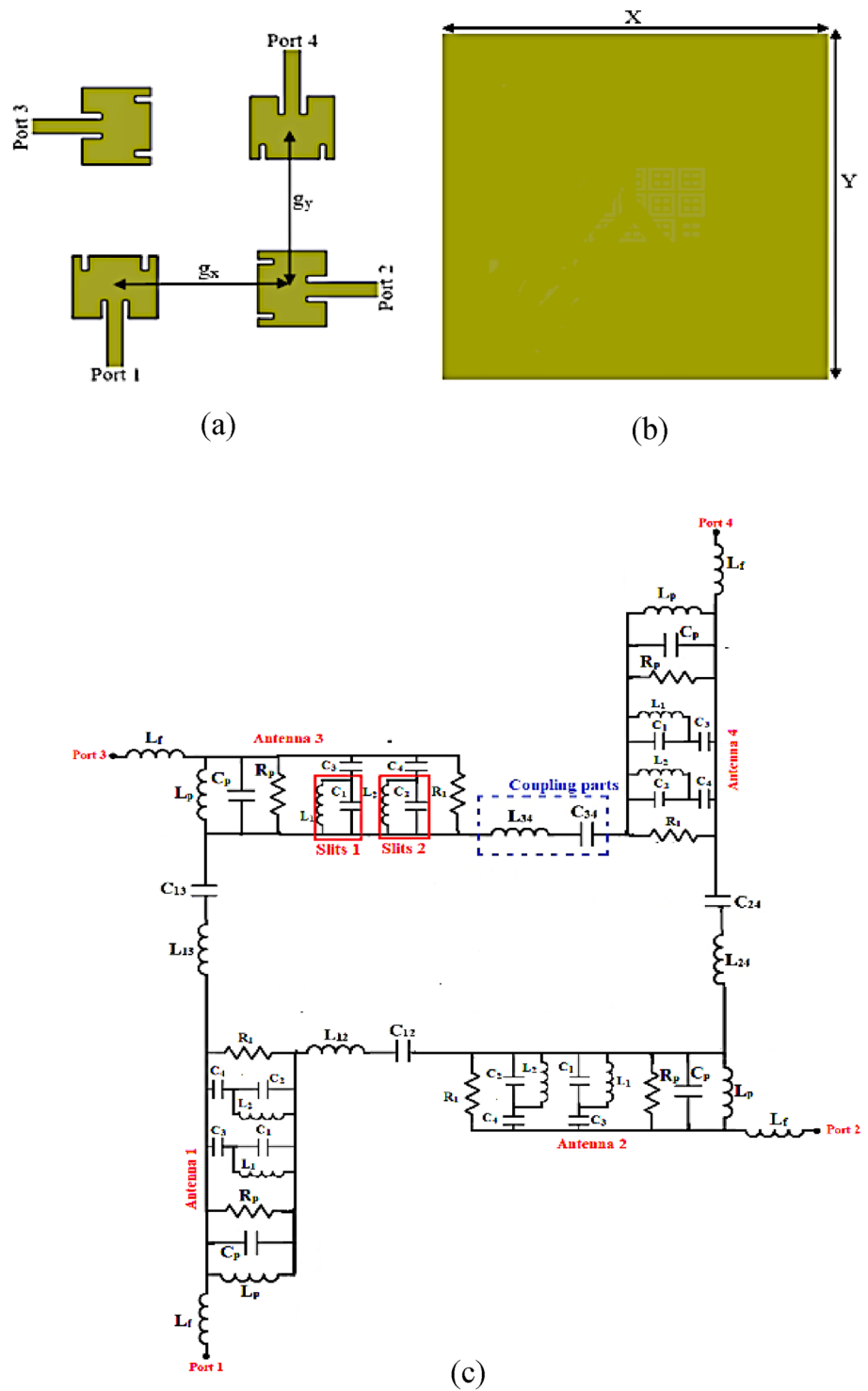
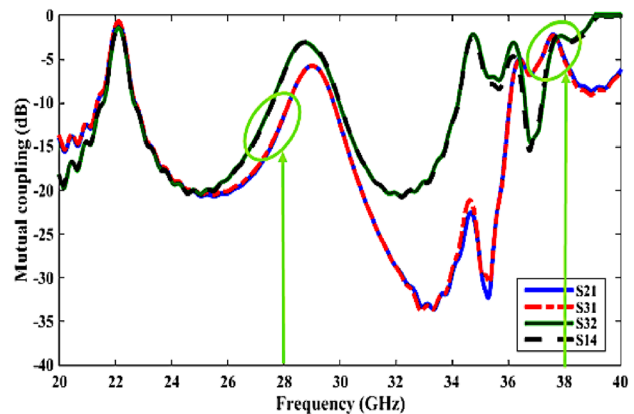


**Table 2** The equivalent circuit parameters of proposed MIMO antenna array

$L_f$	$L_p$	$C_p$	$R_p$	$C_1$	$L_1$	$C_2$	$L_3$	$C_3$	$C_4$	$R_1$
9.4 pH	10.6 pH	3.85 pF	50 $\Omega$	0.2 PF	9.4 pH	8.4 pF	10.4 pH	2 pF	0.6 pF	50 $\Omega$
$L_{12}$	$C_{12}$	$L_{13}$	$C_{13}$	$L_{34}$	$C_{34}$	$L_{24}$	$C_{24}$			
9.2 pH	4 pF	8.9 pH	3.6 pF	8.7 pH	6.75 pF	10 pH	4 pF			

**Fig. 6** Simulated mutual coupling between ports in the absence of any decoupling methods



assessed by varying the value of ( $W_c$ ). Figure 3b illustrates the simulated return loss as ( $W_c$ ) varies, with values of 0.1, 0.3, and 0.6 mm, respectively. Consequently, a ( $W_c$ ) value of 0.3 mm has been selected to provide a  $-10$  dB bandwidth at both 28 GHz and 38 GHz while maintaining a compact configuration.

Figure 4(a) displays the antenna reflection coefficient simulation and measurement results for the two resonance frequencies. It shows the simulated  $S_{11}$  values (lower than  $-10$  dB) for the first band, which ranged from 27.66 GHz to 28.378 GHz, and the second band, which ranged from 37.7 GHz to 38.26 GHz. While the measured  $S_{11}$  findings (lower than  $-10$  dB) for the first band spanned from 27.78 GHz to 28.5 GHz and the second band from 37.81 to 38.37 GHz. Owing to imperfections in the manufacturing process and measurement setup, the simulated outcomes closely matched the measured results, with only slight variations. According to Fig. 4(b), the antenna's gain is 7.8 dBi at 28 GHz and 6.5 dBi at 38 GHz, respectively.

### 3 Mutual coupling in MIMO

The structure of a quad-port MIMO antenna and the techniques used to improve isolation between elements are covered in this section. To achieve high isolation between ports, DS has been sited among elements. The dimensions of every four-port MIMO array design that has been proposed are  $17.76 \text{ mm} \times 17.76 \text{ mm} \times 1.52 \text{ mm}$ . Four instances of the single antenna unit described in the previous section are positioned at a separation of  $g_x = g_y = 5 \text{ mm}$  from one another, oriented orthogonally, as depicted in Fig. 5. The Rogers TMM4 substrate, is the foundation for the proposed antenna array. CST Microwave Studio 2019 is used to simulate the antenna array.

In Fig. 5(c), you can observe the representation of an equivalent resonance circuit model for the MIMO system with four orthogonal elements. Each element is independently connected to a  $50 \Omega$  terminal. It's important to acknowledge that there is always some level of coupling between adjacent antennas. This coupling is represented using LC series lumped elements, and the specific component values are detailed in Table 2. Figure 6 illustrates the MC between ports in a Quad-port MIMO array when no isolation techniques are applied, revealing insufficient isolation within the desired frequency range.

#### 3.1 Utilizing the DS Technique for the design of a four-port MIMO with low MC

Enhancing the MIMO parameters is a crucial objective in the development of 5G millimeter wave wireless terminals. The utilization of the DS structure is recommended to improve these characteristics. Rogers TMM4 material, which has a typical thickness of 1.52 mm ( $\epsilon = 4.5$ ), is the foundation for the proposed antenna array. The suggested antenna system is shown in Fig. 7 using the DS approach, and its sizes are listed as follows:  $w_d = l_d = 2 \text{ mm}$ ,  $s_d = 6 \text{ mm}$ , and  $g_d = l_d = 0.25 \text{ mm}$ .

The suggested array has the following dimensions:  $17.76 \text{ mm} \times 17.76 \text{ mm} \times 1.52 \text{ mm}$ . The electrical circuit model that is equivalent to the antenna array, with the inclusion of the DS, can be observed in Fig. 7(c). The equivalent circuit of the DS is represented by inductance  $L_{DS}$ , capacitance  $C_{DS}$  and reactance  $R_{DS}$ , whose value relies on the space among the radiators.



**Fig. 7** A quad-port MIMO antenna geometry with DS shown in **a** from the top view, **b** from the bottom view, **c** represented as its equivalent circuit, **d** Design Stages of the MIMO antenna, and **e** step-2 Mutual coupling

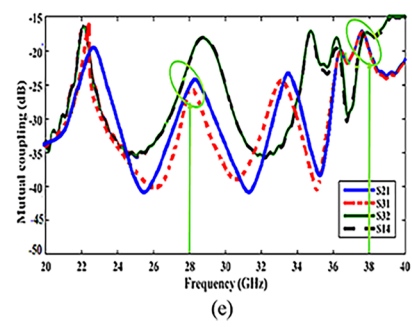
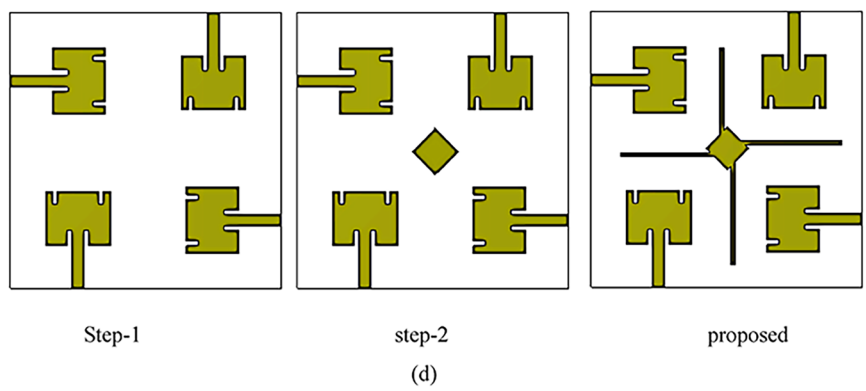
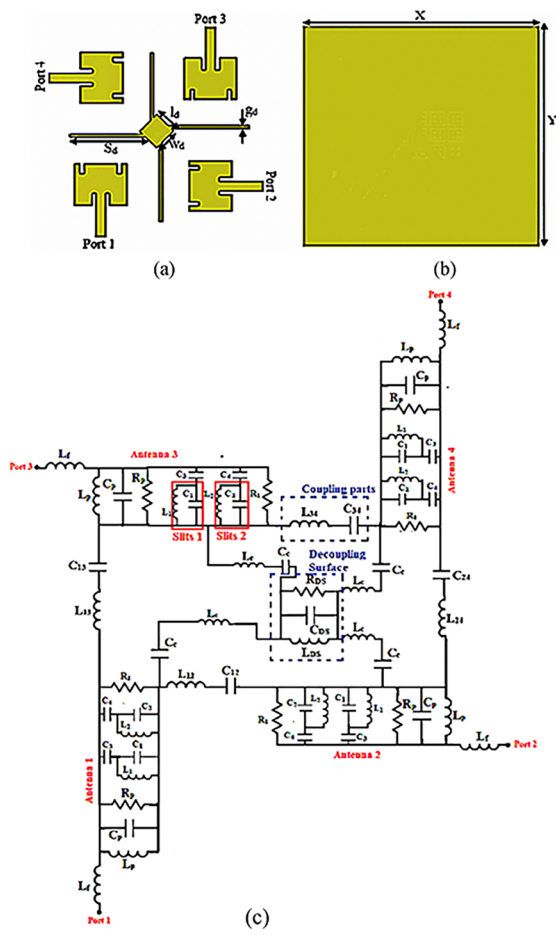


**Table 3** The equivalent circuit parameters of proposed MIMO antenna array

$L_f$	$L_p$	$C_p$	$R_p$	$C_1$	$L_1$	$C_2$	$L_3$	$C_3$	$C_4$	$R_1$	$C_{DS}$
9.4 pH	10.6 pH	3.85 pF	50 $\Omega$	0.2 pF	9.4 pH	8.4 pF	10.4 pH	2 pF	0.6 pF	50 $\Omega$	3.85 pF
$L_{12}$	$C_{12}$	$L_{13}$	$C_{13}$	$L_{34}$	$C_{34}$	$L_{24}$	$C_{24}$	$L_c$	$C_c$	$R_{DS}$	$L_{DS}$
9.2 pH	4 pF	8.9 pH	3.6 pF	8.7 pH	6.75 pF	10 pH	4 pF	9.4 pH	3.85 pF	50 $\Omega$	10.6 pH

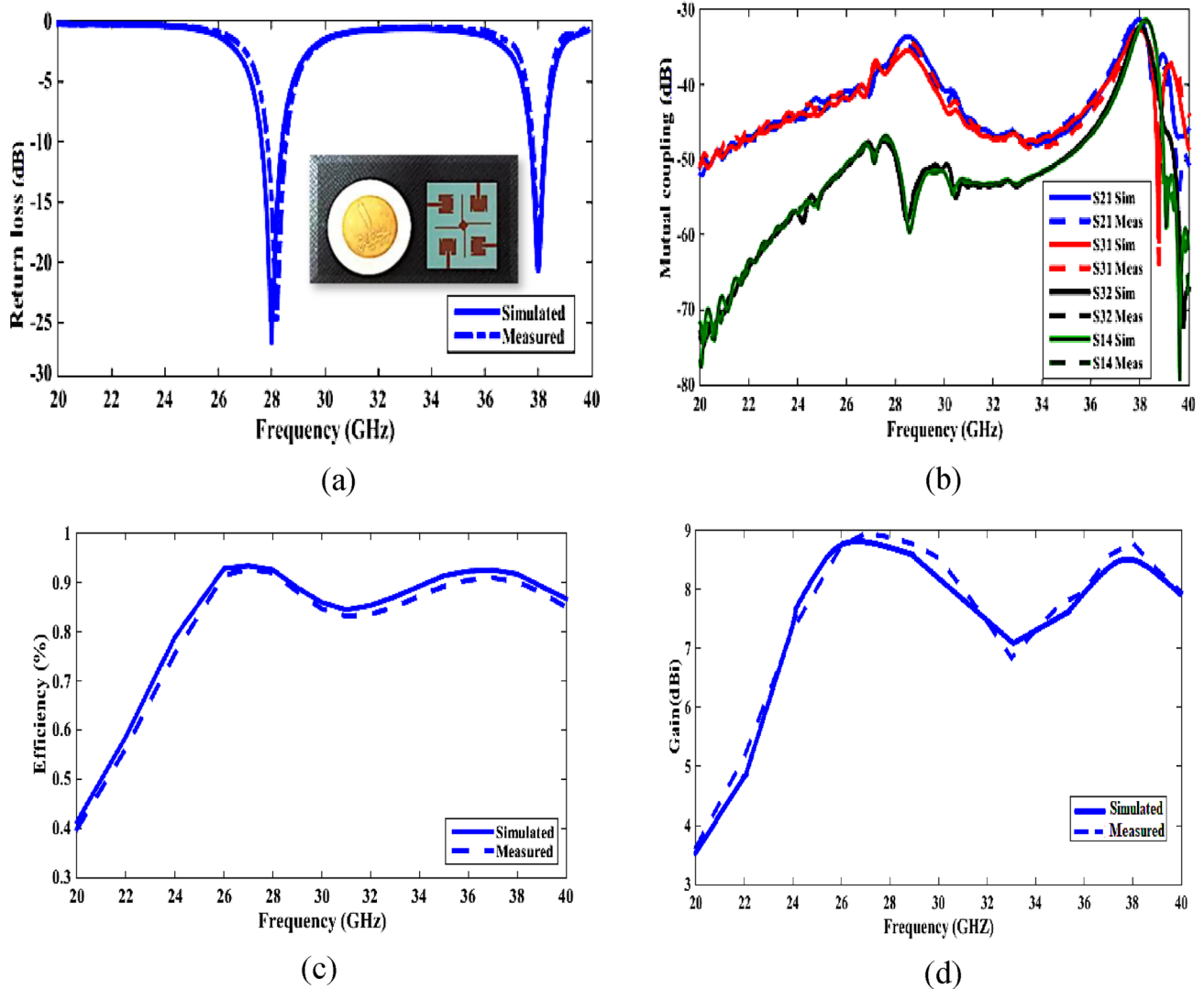


**Fig. 8** Predicated and measured outcomes for quad port MIMO scheme with DS. **a** Return loss, **b** Mutual coupling DS, **c** Efficiency and **d** Gain

The central metallic patch within the array that interconnects the four arms is represented by an inductance ( $L_c$ ). The interaction between the patch and the DS occurs primarily through capacitance ( $C_c$ ), as the DS couples with the patch via the non-radiating edge of the patch antenna. The losses, both ohmic and dielectric, associated with the DS are modeled as resistance  $R_{DS}$ .

We obtained the optimized values for the equivalent circuit model by utilizing a full-wave EM simulation with CST in the 28/38 GHz frequency range. The magnitudes of these parameters can be found in Table 3. The simplified

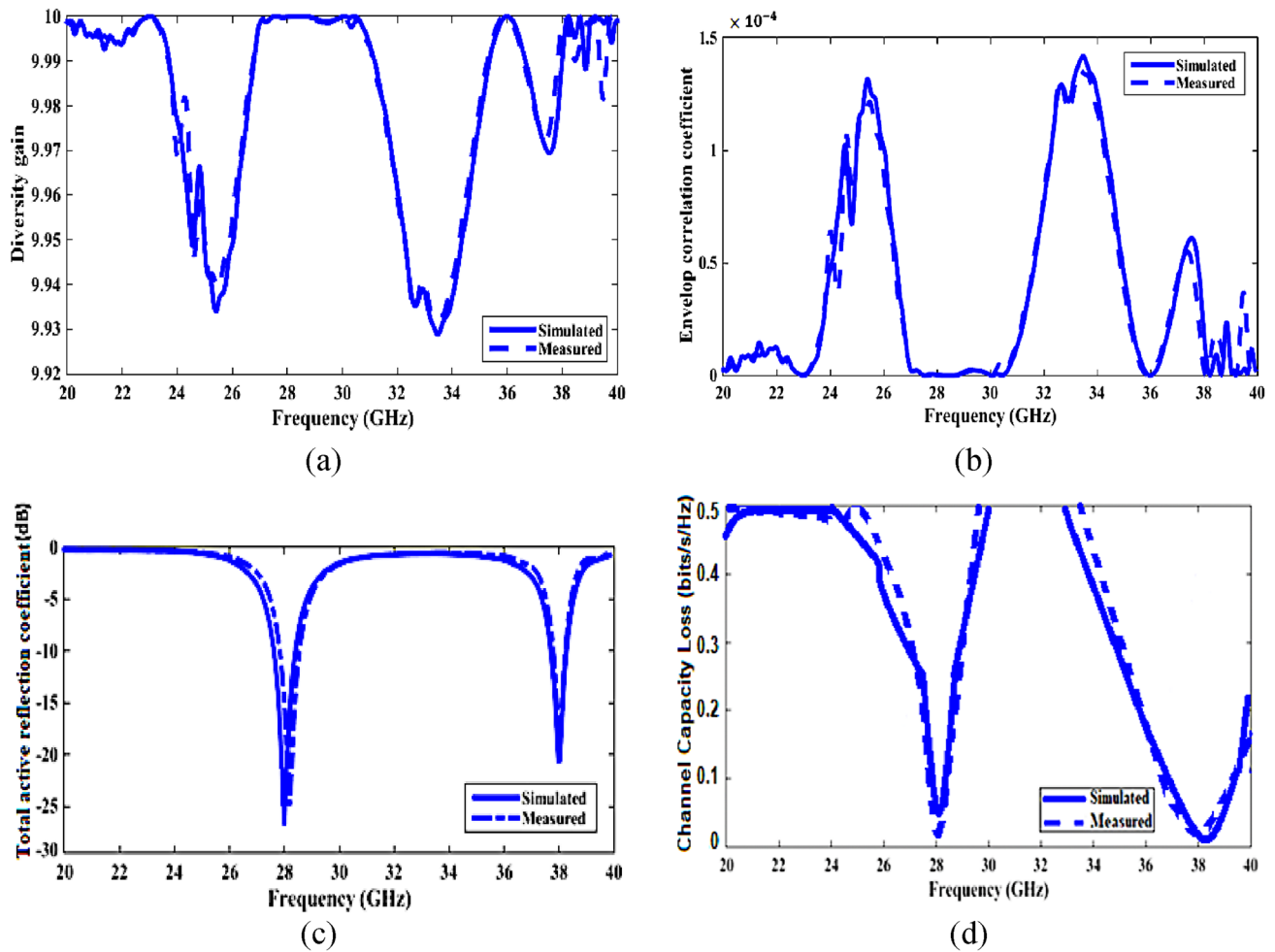
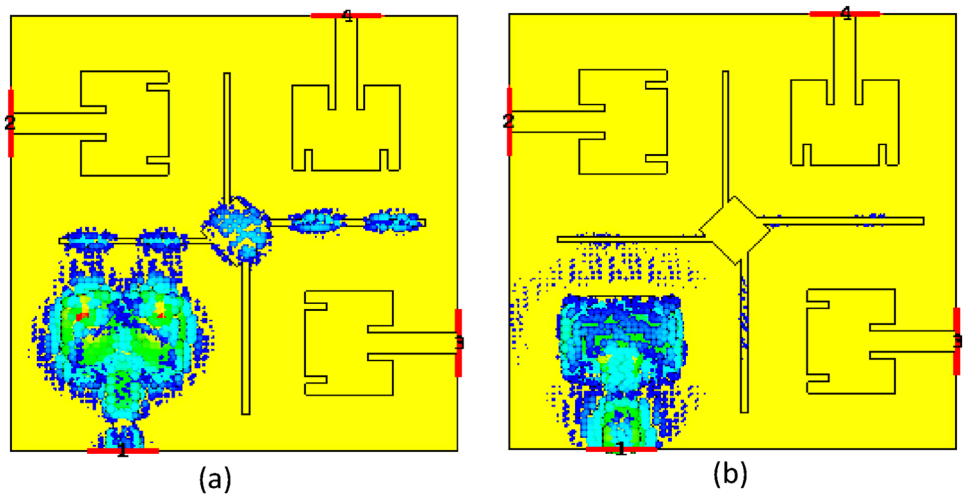


Fig. 9 Predicated and measured outcomes of quad port MIMO antenna with DS **a** ECC, **b** DG, **c** TARC, and **d** CCL

Fig. 10 Current distribution on the surface at (a) 28 GHz and (b) 38 GHz for the port 2 of the four-port MIMO array using DS method



**Table 4** MEG at various frequencies of proposed MIMO antenna array using DS technique

Frequency (GHz)	MEG (dB)	Techniques DS
28	MEG1	− 6.9327
	MEG2	− 6.8925
	MEG3	− 6.125
	MEG4	− 5.998
	MEG1/MEG2	1.0023
	MEG3/MEG4	0.9885
38	MEG1	− 6.9367
	MEG2	− 6.8869
	MEG3	− 6.132
	MEG4	− 5.965
	MEG1/ MEG2	1.0019
	MEG3/ MEG4	0.9865

equivalent circuit model was applied to evaluate the impact of the DS on the return-loss and isolation performance of the antenna array.

Figure 7(d) depicts the MIMO antenna's three primary design stages. The initial design (step-1) for the MIMO array is four copies of the single antenna unit from the previous section are arranged 5 mm apart, orthogonally to one another with dimensions 17.76 mm × 17.76 mm × 1.52 mm and not contain any decoupling techniques. In this stage Fig. 6 shows insufficient isolation within the desired frequency range. From Fig. 6 the mutual coupling at 28 and 38 GHz is around − 15 and − 5 dB respectively. In step-2 the square shaped DS with dimension 2 mm × 2 mm has been added in between antenna element to lessen the mutual coupling. The mutual coupling in this case is poor enhanced as shown in Fig. 7(e). From Fig. 6 the mutual coupling at 28 and 38 GHz is around − 25 and − 20 dB respectively. To farther enhancement four arms is added to square shape as shown in Fig. 7(d). By way of illustrated in Fig. 8(b), the DS approach can produce enough decoupling current to increase isolation to less than—30 dB to—80 dB.

Figure 8(a) depicts the antenna array, which is designed for the fifth generation of millimeter-wave technology and spans the dual bands of 28 GHz and 38 GHz. By way of illustrated in Fig. 8(b), the DS approach can produce enough decoupling current to increase isolation to less than—30 dB. As demonstrated in Fig. 8(c), (d), the efficiency varies around 93% and the gain around 8.9 dBi. DG and ECC are depicted in Fig. 9(a) and (b) to be around 10 and less than  $1.5 \times 10^{-4}$ , respectively. According to Fig. 9(c), the MIMO array's TARC parameter is less than − 20 dB. The CCL of the suggested MIMO array is presented in Fig. 9(d). CCL is satisfied because it is fewer than the intended value of 0.03 bits/s/Hz. To further substantiate the impact of the DS on the antenna performance. In Fig. 10, the surface current distributions are displayed. Following the incorporation of the DS, the majority of the current is concentrated near the central square element and its connecting lines. Additional antenna components display limited current induction, resulting in a reduction of mutual coupling.

### 3.2 MIMO antenna performance evaluation

To analyze the MIMO antenna's performance, various parameters are used. ECC is one of the primary dynamic characteristics used to calculate the MIMO antenna's performance.

One of the most important performance indicators for the MIMO scheme is ECC. The following equation [17] can be used to compute it from the S-parameters:

$$ECC = \frac{|S_{ii} * S_{ij} + S_{ji} * S_{jj}|^2}{(1 - |S_{ii}|^2 - |S_{jj}|^2) * (1 - |S_{jj}|^2 - |S_{ii}|^2)} \quad (14)$$

According to Fig. 9 (b), the results of ECC using DS scheme are approximately less than  $1.5 \times 10^{-4}$ . As soon as the diversity technique is used on the MIMO scheme, DG is the transmission power loss that results. With the help of the following equation [18], DG is calculated:

$$DG = 10\sqrt{1 - (ECC)^2} \quad (15)$$

According to Fig. 9 (a), DG is approximately 10 dB.

TARC represents the third element that follows the port-to-port coupling. TARC is a metric used for assessing the performance of a MIMO antenna, calculated as the ratio of the square root of the total reflected power to the square root of the full incident power. The formula [18] below can be employed to compute TARC:

$$\Gamma = \sqrt{\frac{|s_{ii} + s_{ij}e^{j\theta}|^2 + |s_{ji} + s_{jj}e^{j\theta}|^2}{2}} \quad (16)$$

With a step increment of  $30^\circ$ ,  $\theta$  is the input phase angle in this case from  $0^\circ$  to  $180^\circ$ . Ports 1 and 2's reflection coefficients are  $s_{ii}$  and  $s_{jj}$ , respectively. Figure 9 (c) for proposed design using DS approach display TARC.

Mean Effective Gain (MEG), the fourth parameter, considers the combined factors of overall efficiency, gain, and the calculation of antenna mismatches. MEG values, denoted as MEG1 for antenna #1, MEG2 for antenna #2, MEG3 for antenna #3, and MEG4 for antenna #4, vary within the range of 0.9865 to 1.0091. According to Table 4, MEG for every antenna varieties from -5.923 to -6.9367 dB. Utilizing the following equation [43], the MEG is calculated:

$$MEGi = 0.5\eta_{rad} = 0.5(1 - \sum_{j=1}^k |s_{ij}|^2) \quad (17)$$

In this context, 'K' represents the overall count of antennas, 'l' pertains to the specific active antenna under consideration, and ' $\eta_{rad}$ ' denotes the radiation efficiency of that particular antenna within the scenario involving four antennas."

$$MEG1 = 0.5(1 - |S_{11}|^2 - |S_{12}|^2 - |S_{13}|^2 - |S_{14}|^2) \quad (17a)$$

$$MEG2 = 0.5(1 - |S_{21}|^2 - |S_{22}|^2 - |S_{23}|^2 - |S_{24}|^2) \quad (17b)$$

$$MEG3 = 0.5(1 - |S_{31}|^2 - |S_{32}|^2 - |S_{33}|^2 - |S_{34}|^2) \quad (17c)$$

$$MEG4 = 0.5(1 - |S_{41}|^2 - |S_{42}|^2 - |S_{43}|^2 - |S_{44}|^2) \quad (17d)$$

The MEG measurements should have a range that encompasses.

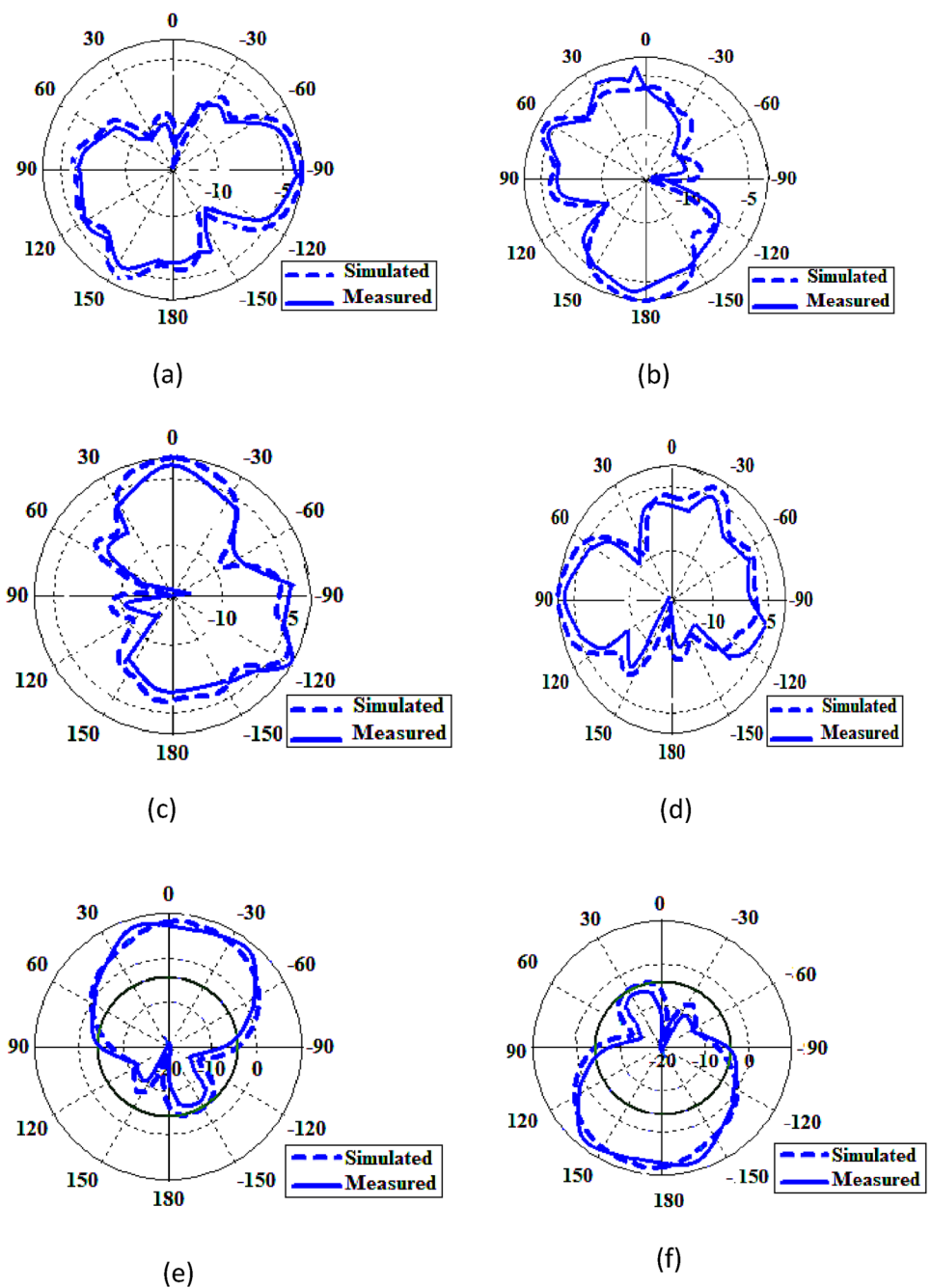
$$-3 \leq MEG(dB) < -12 \quad (18)$$

Channel Capacity Loss (CCL), the fifth performance parameter, is one of the key measures for MIMO. Using the following equation [44], CCL is calculated:

**Table 5** The evaluation of DS based design

Parameter	Techniques DS
Isolation improvement (dB)	At 28 GHz < -35 : -60 At 38 GHz < -35
ECC	< $1.5 \times 10^{-4}$
DG	9.99
Average MEG for each port (dB)	-6.092
TARC (dB)	< -25
Gain (dBi)	8.9at 28 GHz 8.7 at 38 GHz
Efficiency	90%

**Fig. 11** Predicted and measured radiation patterns at  $\theta=90^\circ$ , with a frequency of 28 GHz, including: **a** port (1), **b** port (2), **c** port (3), **d** port (4). Additionally, at  $\varphi=0$  degrees, and a frequency of 28 GHz: **e** port (1), and **f** port (4)



$$Closs = -\log_2(\Psi^R) \tag{19}$$

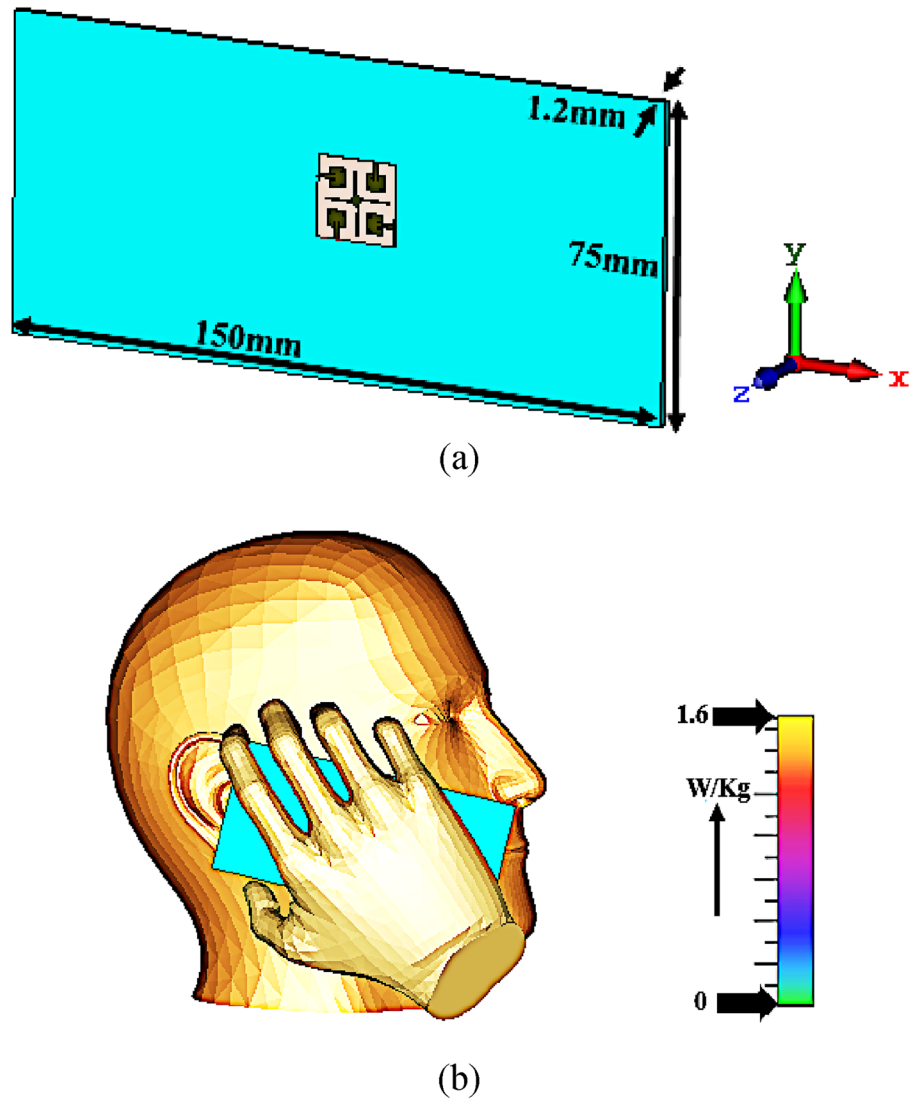
where  $\Psi^R$  is the receiving antenna's correlation matrix, which is written as follows:

$$\Psi^R = \begin{pmatrix} \Psi_{ii} & \Psi_{ij} \\ \Psi_{ji} & \Psi_{jj} \end{pmatrix} \tag{20}$$

where,

$$\Psi_{ii} = 1 - (|S_{ii}|^2 - |S_{ji}|^2) \tag{21}$$

**Fig. 12** **a** Antenna schematic with a dielectric back cover, and **b** arrangement for SAR assessment using a head phantom model



$$\Psi_{ij} = -(S_{ii} * S_{jj} + S_{ij} * S_{ji}) \tag{22}$$

$$\Psi_{ji} = -(S_{jj} * S_{ii} + S_{ij} * S_{ji}) \tag{23}$$

$$\Psi_{jj} = 1 - (|S_{jj}|^2 - |S_{ij}|^2) \tag{24}$$

CCL must be fewer than 0.4 bits/s/Hz to be wanted. The three scenarios satisfy CCL because it is smaller than this value. Figure 9(d) display the outcomes of the CCL.

The outcomes of the DS method for minimizing mutual coupling between antenna elements are listed in Table 5. The mutual coupling reduction strategy result in excellent port isolation and gratified MEG, CCL, TARC, DG, and ECC.

The radiation characteristics of the MIMO system under consideration at 28 GHz are presented in Fig. 11, showcasing key features. In Fig. 11(a), (b), (c), and (d), it's evident that the main lobes are oriented at right angles to each other, pointing towards  $\theta = 90$  degrees. The E-plane patterns exhibit a  $90^\circ$  phase difference. In contrast, the H-plane

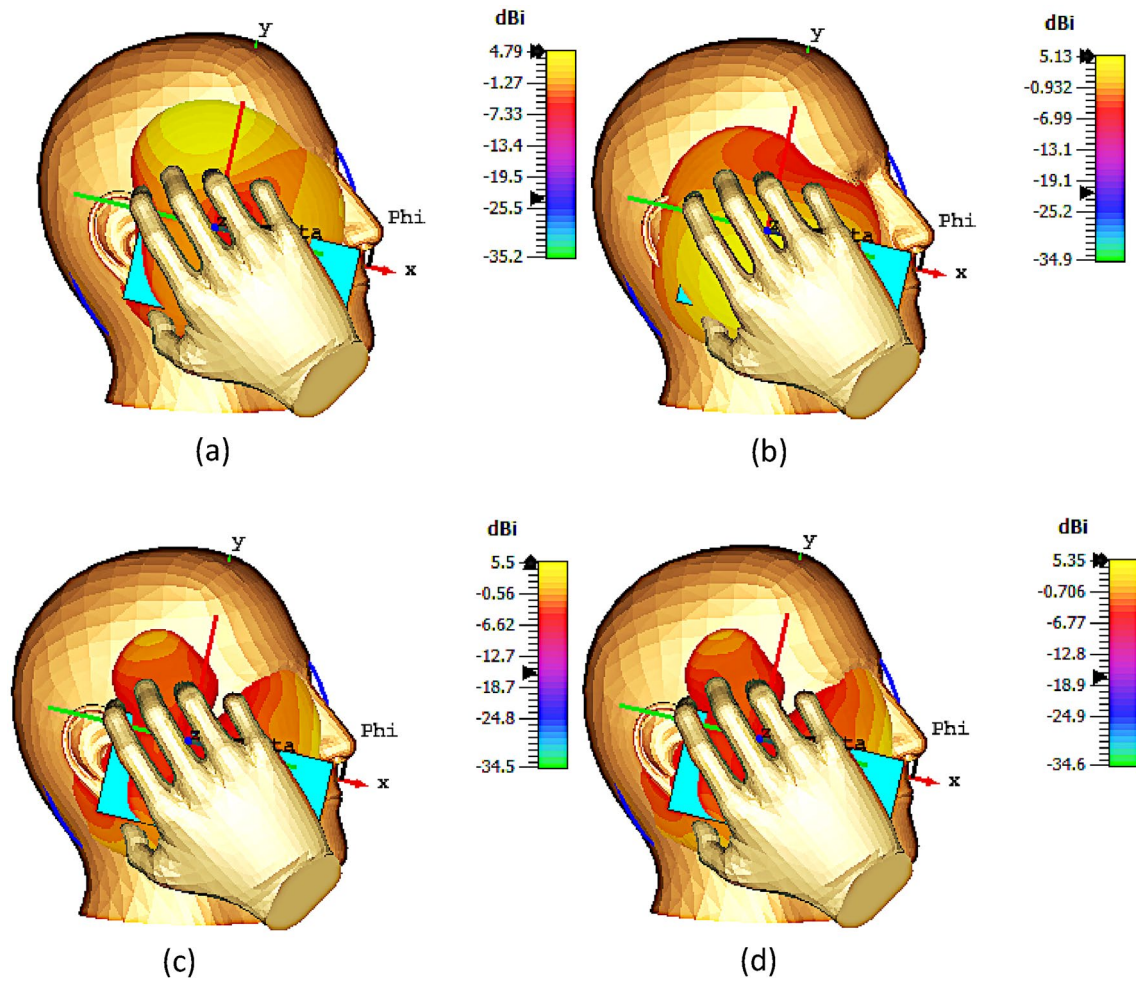


**Fig. 13.** 3D radiation patterns of the finalized MIMO antenna structure with the back cover are simulated at 28 GHz, depicting **a** first port and **b** second port, and at 38 GHz, showcasing **c** first Port and **d** second Port

patterns, as observed in Fig. 11(e) and (f), show a 180° phase difference between antennas #2 and #3, as well as between antennas #1 and #4. Notably, the E-plane patterns closely resemble each other among all antennas.

The measurement of electromagnetic (EM) energy absorbed by the human body during smartphone usage is quantified through a metric known as Specific Absorption Rate (SAR), as explained in references [52] and [55].

Equation (25) provides a definition of SAR as the rate at which electromagnetic energy is absorbed by human tissues per unit of their mass.

$$SAR = \sigma \frac{E_i^2}{\rho} (W/Kg) \tag{25}$$

In this equation,  $\sigma$  stands for the conductivity of the tissue, measured in Siemens per meter (S/m),  $E$  represents the electric field strength in Volts per meter (V/m), and  $\rho$  signifies the tissue's mass density, measured in kilograms per cubic meter (kg/m<sup>3</sup>).

The Specific Absorption Rate (SAR) can be calculated by taking an average over the whole body or a smaller tissue sample, typically 1 g or 10 g. SAR is quantified in watts per kilogram (W/kg) [52]. Given that the suggested MIMO antenna structure is affixed to the back cover, it's essential to predict its Specific Absorption Rate (SAR) value. This back cover is made from a dielectric material with a permittivity of 3.32 and a loss tangent of 0.002. Figure 12(a)



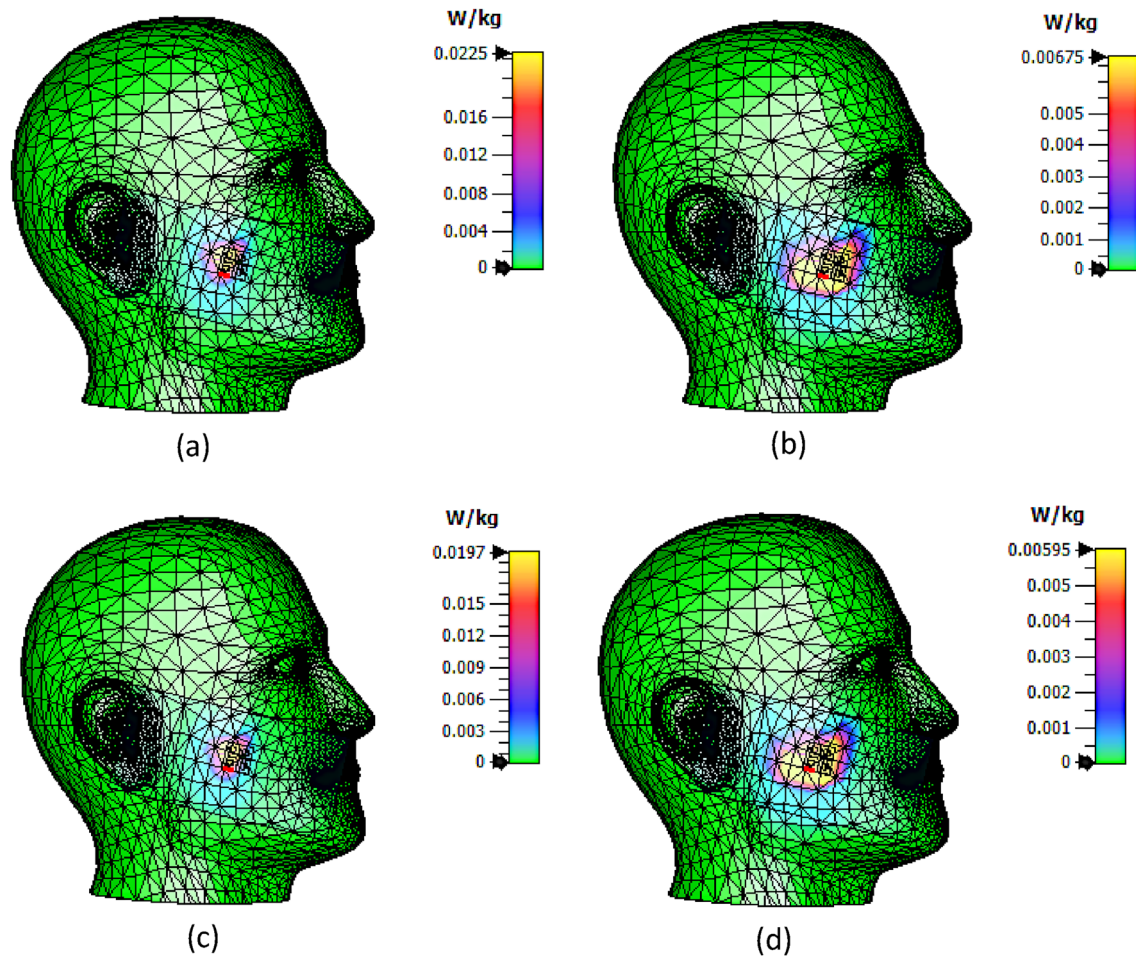


**Fig. 14** SAR simulated at 15 dBm for the proposed MIMO antenna structure with a back cover at 28 GHz, illustrating **a** 1 g and **b** 10 g, and at 38 GHz, depicting **c** 1 g and **d** 10 g

**Table 6** The SAR<sub>1g</sub> and SAR<sub>10g</sub> values obtained through simulation for the proposed MIMO structure with an input power of 15 dBm

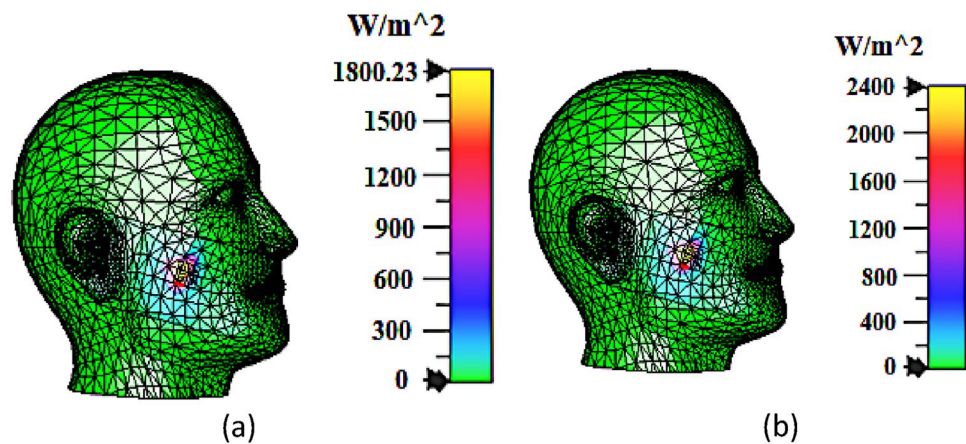
Frequency	Spacing 5 (mm)		Spacing 10 (mm)	
	SAR <sub>1g</sub>	SAR <sub>10g</sub>	SAR <sub>1g</sub>	SAR <sub>10g</sub>
28 GHz	0.0225	0.00576	0.015	0.0031
38GHz	0.00948	0.00332	0.0036	0.0012

**Table 7** The SAR<sub>1g</sub> and SAR<sub>10g</sub> values obtained through simulation for the proposed MIMO structure with an input power of 20 dBm

Frequency	Spacing 5 (mm)	
	SAR <sub>1g</sub>	SAR <sub>10g</sub>
At 28 GHz	0.057	0.036
At 38GHz	0.023	0.00945

illustrates the antenna’s configuration with the back cover, which has dimensions of  $150 \times 70 \times 1.2 \text{ mm}^3$ . Figure 12(b) shows the setup designed to assess the electromagnetic energy absorbed by a human head, employing a human head phantom model. The antenna is oriented at 650 with reference to the negative vertical axis. Highlighting the significance of the SAR value, it is greatly influenced by the spatial gap between the antenna patch and various parts

**Fig. 15** Simulated power density for the proposed MIMO antenna structure with a back cover at: **a** 28 GHz, **b** 38 GHz



of the human body [52]. In our study, the simulation positions the MIMO antenna 5 mm away from the head phantom model, specifically near the ear and mouth regions of the head phantom model.

Following the FCC regulations, the input power for radiators used in 5G configurations can be set at 15 dBm, 18 dBm, and 20 dBm, maintaining a 5 mm separation among the head and the radiator [55]. Figure 13 showcases the radiation patterns of the antenna when a human head model, a hand model, and a rear antenna with a back cover are included in the setup for an input power of 15 dBm. Figure 14, shows the simulated value of SAR1g and SAR10g at 28 GHz and 38 GHz for 15 dBm when port 1 is active and the other three ports is inactive.

Figure 14 data clearly shows that SAR is more pronounced at shorter distances from the antennas when compared to greater distances. SAR1g registers higher values than SAR10g, as indicated in Table 6, highlighting that SAR diminishes as the separation between the antenna and the human head and hand model increases. The simulation outcomes for SAR1g and SAR10g at 28/38 GHz with an input power of 15 dBm are presented in Table 6. These findings indicate that the SAR1g values comfortably fall within permissible thresholds, with all simulated values adhering to the SAR limits defined by FCC and ICNIRP standards, which are set at 1.6 W/Kg.

As per Eq. (25), the SAR values are contingent upon the electric field strengths (E) of the antennas. The simulation outcomes in Table 7, involving an input power of 20 dBm, reveal SAR values that fall within lower ranges than anticipated. Given the potential risks associated with electromagnetic fields and their impact on human tissues, it is advantageous to devise antennas with low SAR values for mobile handsets, especially when these devices are utilized in close proximity to the human body. This approach serves to mitigate any potential adverse health effects.

As shown in Fig. 15, the power densities (PD) were computed numerically at an input power of 1 W. 1800.23 W/m<sup>2</sup> at 28 GHz and 2400 W/m<sup>2</sup> at 38 GHz were the top power densities. It is clear that the suggested MIMO antenna needs to be positioned 5 mm away from the human head in order to function within safety parameters with an input power of 1 W. However, because the Maximum Effective Isotropic Radiated Power (EIRP) is in the mW range, which is much smaller than 1 W, in practice the transmitter's radiated power is likewise limited. Even when positioned directly above the skin, the suggested MIMO antenna is safe as long as its DS and input power are within milliwatt ranges. The computed power density for the suggested MIMO antenna construction with a 28 GHz and 38 GHz rear cover is displayed in Fig. 15.

#### 4 Comparison with related works

Despite attempts to produce a dual-band MIMO antenna with high isolation, design considerations like the low profile and improved gain make it challenging to sacrifice the compact size. In this paper, a 5G Millimeter-Wave 28/38 GHz dual-band MIMO antenna array is introduced. The designed configuration is tailored for 5G Millimeter-Wave wireless terminals. The finalized MIMO antenna array exhibits exceptional attributes and performance, including its compact form, port count, frequency coverage, minimum coupling, enhancement in minimum coupling, gain, efficiency, error correction capability, and directivity. These characteristics surpass those found in designs #1 through #16. A comparative analysis reveals a competitive edge in the provided MIMO antenna array configurations, which are summarized in Table 8.

**Table 8** Comparative analysis of the performance between the proposed design and previous studies

No	Refs.	Dimension (mm <sup>2</sup> )	Ports No	Frequency band (GHz)	MC scheme	MC improvement (dB)	Peak gain (dBi)	Radiation efficiency (%)	ECC	DG
#1	[2]	60 × 60	4	28/38	DGS	< -30	8.14/8.07	NA	10 <sup>-3</sup>	9.89
#2	[10]	26 × 11	2	28/37	NA	< -31 / -24	5.1/5.8	98.9/99	10 <sup>-4</sup>	9.98
#3	[15]	38 × 83	6	4.8	DGS	-48	6.45	86	0.029	9.88
#4	[17]	29 × 33	2	28/38	Two NL + CSRR	-59.9/-28.2	8.9	97	6.5 × 10 <sup>-8</sup>	9.99
#5	[18]	34 × 55	2	28/38	EBG	< -22 : 59	NA	96	5.5 × 10 <sup>-5</sup>	9.99
#6	[25]	20 × 20	4	28/37	NA	< -16.2 / -12.1	7.1	NA	NA	9.7
#7	[27]	43 × 43	4	28/37	DGS	< -19.9 / -31	7.9	NA	2.4 × 10 <sup>-4</sup>	9.978
#8	[28]	41 × 8.2	4	28/38	NA	< -24.8	5.6	86	0.0035	9.89
#9	[45]	63 × 63	2	3.5	DS	< -22	7.1	95	0.002	9.9
#10	[46]	30 × 15	2	28/38	EBG	< -32	5.7	NA	10 <sup>-4</sup>	10
#11	[47]	20 × 20	4	28/38	DGS	< -24	6	83	< 0.0001	9.99
#12	[48]	28 × 28	4	28/38	DS	< -25	4	NA	< 0.001	9.98
#13	[49]	30 × 35	4	28	NA	< -40	8	80	< 0.0003	9.96
#14	[50]	30 × 35	4	25.5/29.6	DGS	< -17	6	80	< 0.01	9.96
#15	[51]	31 × 26	2	1.5-4.5	EBG	< -25	3	NA	NA	NA
#16	[53]	100 × 72	4	3.8/4.2	Metamaterial	< -20	4	95	0.03	9.95
Suggested work		17.76 × 17.76	4	28/38	DS	< -35 : 60	8.9	90	< 1.5 × 10 <sup>-4</sup>	9.99

**Table 9** Comparing SAR values between the proposed design and previous studies at 28 GHz

No	Refs.	Spacing (mm)	Power (dBm)	No. of ports	SAR 1 g	SAR 10 g
#1	[52]	5	15	2	1.18	0.963
			20		1.57	1.36
#2	[56]	5	15	1	1.25	0.31
			20		NA	0.998
#3	[57]	5	24	2	1.352	NA
#4	[58]	NA	NA	NA	1.423	0.3
#5	[59]	NA	24	8	NA	1.23
#6	[60]	NA	NA	2	NA	0.36
Suggested work		5	15	4	0.0225	0.00576
			20		0.00948	0.00332

Table 9 have been included to facilitate a comparison of Specific Absorption Rate (SAR) values. As per Table 9, it's evident that the SAR values for the proposed antenna generally tend to be lower than those reported in prior studies at the 28/38 GHz frequency range.

## 5 Conclusion

Decoupling structure (DS) techniques were employed to reduce mutual coupling, and their effectiveness was evaluated. Using CST STUDIO SUITE version 2019, we simulated the model of the radiating elements with optimum sizes. The suggested MIMO antenna was designed to operate at two resonance frequencies of 28/38 GHz, with isolation better than 30 dB across two operational bands. DS techniques were utilized to improve the isolation between antennas, resulting in a high efficiency of 93% and a gain of 9.7 dBi. To assess the diversity performance of the antenna design and highlight the superiority of the suggested four-port MIMO antenna, we extracted MIMO parameters, including ECC, DG, MEG, and CCL, from a combination of simulation and measurement data. The outcomes from these simulations and tests reveal a favorable trend across the two designated operating bands, indicating that the proposed structure is well-suited for application in 5G millimeter-wave wireless terminals. Moreover, the Specific Absorption Rate (SAR) value within both operating bands falls within the permissible standard limit, which is below 1.6 W/Kg.

**Acknowledgements** The authors express their gratitude to the New Damietta Higher Institute of Engineering and Technology (NDETI), Damietta, Egypt, as well as the University Teknikal Malaysia Melaka (UTeM) and the Ministry of Higher Education of Malaysia (MOHE) for their support in this project.

**Author contributions** R.H. Elabd: Writing—Original draft preparation, Investigation, Validation and Software; A.J.A. Al-Gburi: Conceptualization, Methodology, Data curation, Writing—Reviewing and Editing, Supervision and Validation. All authors reviewed the manuscript.

**Data availability** The data that support the findings of this study are available from the corresponding author upon reasonable request.

## Declarations

**Competing interests** The authors declare no competing interests.

**Open Access** This article is licensed under a Creative Commons Attribution 4.0 International License, which permits use, sharing, adaptation, distribution and reproduction in any medium or format, as long as you give appropriate credit to the original author(s) and the source, provide a link to the Creative Commons licence, and indicate if changes were made. The images or other third party material in this article are included in the article's Creative Commons licence, unless indicated otherwise in a credit line to the material. If material is not included in the article's Creative Commons licence and your intended use is not permitted by statutory regulation or exceeds the permitted use, you will need to obtain permission directly from the copyright holder. To view a copy of this licence, visit <http://creativecommons.org/licenses/by/4.0/>.

## References

1. Nizar S, Anouar B, Islem BH, Lassaad L, Ali G. Millimeter-wave dual-band MIMO antennas for 5G wireless applications. *J Infrared Millimeter Terahertz Waves*. 2023;44:297–312. <https://doi.org/10.1007/s10762-023-00914-5>.
2. Kutay C, Nursel A, Tayfun O, Galip OA. 28/38 GHz dual-band MIMO antenna with wideband and high gain properties for 5G applications. *Int J Electron Commun (AEÜ)*. 2023;162:154553–64.
3. Kumar P, Singh AK, Kumar R, Mahto SK, Pal P, Sinha R, Choubey A, Al-Gburi AJA. Design and analysis of low profile stepped feedline with dual circular patch MIMO antenna and stub loaded partial ground plane for wireless applications progress in. *Electromagn Res*. 2024;140(135):144. <https://doi.org/10.2528/PIERC2312120>.
4. Li CM, Zhang A, Kishk A. Dual-polarized broadband base station antenna backed with dielectric cavity for 5G communications. *IEEE Antennas Wireless Propag Lett*. 2019;18(10):2051–5.
5. Elabd RH, Al-Gburi AJA. Super-compact 28/38 GHz 4-Port MIMO antenna using metamaterial-inspired EBG structure with SAR analysis for 5G cellular devices. *J Infrared Milli Terahz Waves*. 2023. <https://doi.org/10.1007/s10762-023-00959-6>.
6. Parchin NO, Basherlou HJ, Al-Yasi YA, Abdulkhaleq AM, Patwary M, Abd-Alhameed RA. A new CPW-fed diversity antenna for MIMO 5G. *Electronics*. 2020;9:261–76. <https://doi.org/10.3390/electronics9020261>.
7. Ibrahim AA, Ali WAE, Alathbah M, Sabek AR. Four-Port 38 GHz MIMO antenna with high gain and isolation for 5G wireless networks. *Sensors*. 2023;23:3557–76. <https://doi.org/10.3390/s23073557>.
8. Ali A, Munir ME, Marey M, Mostafa H, Zakaria Z, Al-Gburi AJA, Bhatti FA. A compact MIMO multiband antenna for 5G/WLAN/WIFI-6 devices. *Micromachines*. 2023;14(6):1153. <https://doi.org/10.3390/mi14061153>.
9. Shayea I, Tharek AR, Marwan HA, Rafiqul I. Real measurement study for rain rate and rain attenuation conducted over 26 GHz microwave 5G link system in Malaysia. *IEEE Access*. 2018;6:19044–64.
10. Ali W, Sudipta D, Hicham M, Soufian L. Planar dual-band 27/39 GHz millimetre—wave MIMO antenna for 5G applications. *Microsyst Technol*. 2021;27:283–92.
11. Mistri RK, Mahto SK, Singh AK, Sinha R, Al-Gburi AJA, Alghamdi TAH, Alathbah M. Quad element MIMO antenna for C, X, Ku, and Ka-band applications. *Sensors*. 2023;23(20):8563. <https://doi.org/10.3390/s23208563>.
12. Hussain N, Wahaj AA, Wael A, Syeda I, Na AZ, Tuan TL. Compact wideband patch antenna and its MIMO configuration for 28 GHz applications. *AEU Int J Electron Commun*. 2021;132:153612.
13. Ali A, Munir ME, Nasralla MM, Esmail MA, Al-Gburi AJA, Bhatti FA. Design process of a compact tri-band MIMO antenna with wideband characteristics for sub-6 GHz, Ku-band, and millimeter-wave applications. *Ain Shams Eng J*. 2024;15(3): 102579.
14. Jilani SF, Akram A. Millimetre-wave T-shaped MIMO antenna with defected ground structures for 5G cellular networks. *IET Microwaves Antennas Propag*. 2018;12(5):672–7.
15. Akhilesh K, Jyoti M, Prabina P, Dukhishyam S, Ganesh P. Six-port mid-bands Low-SAR MIMO antenna for WLAN, 5G mobile terminals, and C-band applications. *Int J Electron Commun (AEÜ)*. 2023;166:154665–77.
16. Hala MM, Mohamed IA, Abdelhamed AS. A novel dual-band 28/38 GHz slotted microstrip MIMO antenna for 5G mobile applications. *J Electromagn Waves Appl*. 2019;33:1581–90.
17. Elabd RH, Abdullah HH. A high isolation UWB MIMO vivaldi antenna based on CSRR-NL for contemporary 5G millimeter-wave applications. *J Infrared Milli Terahz Waves*. 2022;43:920–41. <https://doi.org/10.1007/s10762-022-00894-y>.
18. Elabd RH, Abdullah HH, Abdelazim M. Compact highly directive MIMO vivaldi antenna for 5G millimeter-wave base station. *J Infrared Milli Terahz Waves*. 2021;42:173–94. <https://doi.org/10.1007/s10762-020-00765-4>.
19. Yang B, Zhiqiang Y, JiLan RZ, Jianyi Z, Wei H. Digital beam forming- based massive MIMO transceiver for 5G millimeter-wave communications. *IEEE Trans Microw Theory Tech*. 2018;66(7):3403–18.
20. Ohyun J, Jung-Ju K, Jungmin Y, Dooseok C, Wonbin H. Exploitation of dual polarization diversity for 5G millimeter-wave MIMO beam forming systems. *IEEE Trans Antennas Propag*. 2017;65(12):6646–55.
21. Mneesy TS, Radwa KH, Amira IZ, Wael AEA. A novel high gain monopole antenna array for 60 GHz millimeter-wave communications. *Appl Sci*. 2020;10(13):4546.
22. Marzouk HM, Mohamed IA, Abdel HS. Novel dualband 28/38 GHz MIMO antennas for 5G mobile applications. *Progress Electromag Res*. 2019;93:103–17.
23. Aliakbari H, Abdolali A, Alessandra C, Diego M, Rashid M, Pedram M. ANN-based design of a versatile millimetre-wave slotted patch multi-antenna configuration for 5G scenarios. *IET Microwaves Antennas Propag*. 2017;11(9):1288–95.
24. Hasan MN, Bashir S, Chu S. Dual band omnidirectional millimeter wave antenna for 5G communications. *J Electromag Waves Appl*. 2019;33(12):1581–90.
25. Ikram M., Yifan W., Mohammad S. Sh., and Amin A. Dual band circular MIMO antenna system for 5G wireless devices, In 2018 IEEE International Symposium on Antennas and Propagation & USNC/URSI National Radio Science Meeting, pp. 247–248. 2018.
26. Omar A, Mousa H, Rajmohan IJ, Ba Kh. Dual-band MIMO coplanar waveguide-fed-slot antenna for 5G communications. *Heliyon*. 2021;7(4):6779.
27. Aghoutane B, Sudipta D, Mohammed EGH, Madhav BTP, Hanan EF. A novel dual band high gain 4-port millimeter wave MIMO antenna array for 28/37 GHz 5G applications. *AEU-Int J Electron Commun*. 2022;145(4): 154071.
28. Rafique U, Shobit A, Nasir N, Hisham Kh, Khalil U. Inset-fed planar antenna array for dual-band 5G MIMO applications. *Progress In Electromag Res C*. 2021;112:83–98.
29. Farahat AE, Khalid FAH. 28/38 GHz dual-band Yagi-Uda antenna with corrugated radiator and enhanced reflectors for 5G MIMO antenna systems. *Progress Electromag Res C*. 2020;101:159–72.
30. Liu P, Xiao-W Z, Yan Z, Xiang W, Chunfeng Y, Zhi HJ. Patch antenna loaded with paired shorting pins and H-Shaped slot for 28/38 GHz dual-band MIMO applications. *IEEE Access*. 2020;8:23705–12.
31. Farahat AE, Khilaid FH. Dual-band (28/38 GHz) MIMO antenna system for 5G mobile communications with efficient DoA estimation algorithm in noisy channels. *Appl Computat Electromag Soc J (ACES)*. 2021;36(3):282–94.

32. Marzouk HM, Ahmed MI, Shaalan AA. A novel dual-band 28/38 GHz AFSL MIMO antenna for 5G smartphone application. *J Phys Conf Ser.* 2020;1447:1.
33. Gómez L, Ibrahim AS. Design, analysis and simulation of microstrip antenna arrays with flexible substrate in different frequency, for use in UAV-assisted marine communications. *J Mar Sci Eng.* 2023;11:730. <https://doi.org/10.3390/jmse11040730>.
34. Wu W, Yuan B, Wu A. A quad-element UWB-MIMO antenna with band-notch and reduced mutual coupling based on EBG structures. *Int J Antennas Propag.* 2018;2018:8490740.
35. Roy S, Chakraborty U. Mutual coupling reduction in a multi-band MIMO antenna using meta-inspired decoupling network. *Wireless Pers Commun.* 2020;114(4):3231–46.
36. Anitha R, Vinesh PV, Prakash KC, Mohanan P, Vasudevan K. A compact quad element slotted ground wideband antenna for MIMO applications. *IEEE Trans Antennas Propag.* 2016;64(10):4550–3.
37. Kulkarni J, Desai A, Sim C-Y-D. Wideband four-port MIMO antenna array with high isolation for future wireless systems. *AEU- Int J Electron Commun.* 2021;128:153507. <https://doi.org/10.1016/j.aeue.2020.153507>.
38. Zou X-J, Wang G-M, Wang Y-W, Zong B-F. Mutual coupling reduction of quasi-yagi antenna array with hybrid wideband decoupling structure. *AEU-Int J Electron Commun.* 2021;129:153553.
39. Birwal A, Singh S, Kanaujia BK, Kumar S. MIMO/diversity antenna with neutralization line for WLAN applications. *Mapan.* 2021;36:763–72.
40. Zhang S, Pedersen GF. Mutual coupling reduction for UWB MIMO antennas with a wideband neutralization line. *IEEE Antennas Wireless Propag Lett.* 2016;15:166.
41. Khan MS, Capobianco A-D, Shaque MF, Ijaz B, Naqvi A, Braaten BD. Isolation enhancement of a wideband MIMO antenna using parasitic elements. *Microw Opt Technol Lett.* 2015;57(7):1677–82.
42. Yang M, Zhou J. A compact pattern diversity MIMO antenna with enhanced bandwidth and high-isolation characteristics for WLAN/5G/WiFi applications. *Microw Opt Technol Lett.* 2020;62(6):2353.
43. Ding K, Gao C, Qu D, Yin Q. Compact broadband MIMO antenna with parasitic strip. *IEEE Antennas Wireless Propag Lett.* 2017;16:2349–53.
44. Sultan KS, Abdullah HH. Planar UWB MIMO-diversity antenna with dual notch characteristics. *Prog Electromagn Res C.* 2019;93:119–29.
45. Kartha MM, Jayakumar M. Circularly polarized stub-loaded annular ring patch antenna for 2x2 MIMO satellite application. *Measurement.* 2023;217:113044–56. <https://doi.org/10.1016/j.measurement.2023.113044>.
46. Ali WA, Ibrahim AA, Ahmed AE. Dual-band millimeter wave 2 x 2 MIMO Slot antenna with low mutual coupling for 5G networks. *Wirel Pers Commun.* 2023;129:2959–76.
47. Sghaier N, Belkadi A, Hassine IB, Latrach L, Gharsallah A. Millimeter-wave dual-band MIMO antennas for 5G wireless applications. *J Infrared Millim Terahertz Waves.* 2023;44:297–312.
48. Hussain M, Awan WA, Ali EM, Alzaidi MS, Alsharif M, Elkamouchi DH, Alzahrani A, Sree FA. Isolation improvement of parasitic element-loaded dual-band MIMO antenna for mm-wave applications. *Micromachines.* 2022;13:1918.
49. Bilal M, Naqvi SI, Hussain N, Amin Y, Kim N. High-Isolation MIMO antenna for 5G millimeter-wave communication systems. *Electronics.* 2022;11:962.
50. Khalid M, Iffat Naqvi S, Hussain N, Rahman M, Mirjavadi SS, Khan MJ, Amin Y. 4-Port MIMO antenna with defected ground structure for 5G millimeter wave applications. *Electronics.* 2020;9:71.
51. Nikam PB, Jayendra Kumar V, Sivanagaraju AB. Dual-band reconfigurable EBG loaded circular patch MIMO antenna using defected ground structure (DGS) and PIN diode integrated branch-lines (BLs). *Measurement.* 2022;195(111127):111137. <https://doi.org/10.1016/j.measurement.2022.111127>.
52. Elabd RH, Al-Gburi AJA. SAR assessment of miniaturized wideband MIMO antenna structure for millimeter wave 5G smartphones. *Microelectron Eng.* 2023;282:112098–115. <https://doi.org/10.1016/j.mee.2023.112098>.
53. Dwivedi AK, Sharma A, Singh AK, Singh V. Metamaterial inspired dielectric resonator MIMO antenna for isolation enhancement and linear to circular polarization of waves. *Measurement.* 2021;182(109681):109693. <https://doi.org/10.1016/j.measurement.2021.109681>.
54. Iqbal A, Bouazizi A. Dielectric resonator antenna with top loaded parasitic strip elements for dual-band operation *Microw. Opt Technol Lett.* 2019;61(9):2134.
55. Pant A, Singh M. and manoj singh parihar "a frequency reconfigurable/switchable MIMO antenna for LTE and early 5G applications. *Int J Electron Commun.* 2021;131:153638.
56. Lak A, Adelpour Z, Oraizi H, Parhizgar N. Design and SAR assessment of three compact 5G antenna arrays. *Sci Rep.* 2021;11:21265.
57. Umar Farooq GM, Rather A. Miniaturised Ka/V dual band millimeter wave antenna for 5G body centric network applications. *Alexandria Eng.* 2022. <https://doi.org/10.1016/j.aej.2022.01.044>.
58. Zada M, Ali Shah I, Yoo H. Integration of sub-6-GHz and mm-wave bands with a large frequency ratio for future 5G MIMO applicati. *IEEE Access.* 2021;9:11241–51.
59. OjaroudiParchin N, et al. MM-wave phased array Quasi-Yagi antenna for the upcoming 5G cellular communications. *Appl Sci.* 2019. <https://doi.org/10.3390/app9050978>.
60. Khan J, Sehrai DA, Ali U. Design of dual band 5G antenna array with SAR analysis for future mobile handsets. *J Electr Eng Technol.* 2018;14(2):809–16.

**Publisher's Note** Springer Nature remains neutral with regard to jurisdictional claims in published maps and institutional affiliations.